# Integrity with LiDAR Incorrect Extraction Faults in Adverse Weather Conditions

Kana Nagai, Sahil Ahmed, Boris Pervan, *Illinois Institute of Technology*

## BIOGRAPHY

**Kana Nagai** is currently a Ph.D. candidate and research assistant in Mechanical and Aerospace Engineering at Illinois Institute of Technology (IIT). She received her M.S. and B.S. in Mechanical Engineering from IIT and B.E. in Architecture from Hokkaido University, Japan.

**Sahil Ahmed** is currently a Ph.D. Candidate at the Navigation Laboratory in Mechanical and Aerospace Engineering at IIT. He also works as a Pre-Doctoral Researcher at Argonne National Laboratory. His research interests include Spoofing Detection in GNSS receivers, Software-Defined Radios (SDR), Satellite Communication, Statistical Signal Processing, Estimation and Tracking, and Sensor Fusion for autonomous systems.

**Dr. Boris Pervan** is a Professor of Mechanical and Aerospace Engineering at IIT, where he conducts research on advanced navigation systems. Prior to joining the faculty at IIT, he was a spacecraft mission analyst at Hughes Aircraft Company (now Boeing) and a postdoctoral research associate at Stanford University. Prof. Pervan received his B.S. from the University of Notre Dame, M.S. from the California Institute of Technology, and Ph.D. from Stanford University.

## ABSTRACT

This paper examines adverse weather impacts on the safety of LiDAR-based navigation for self-driving cars. Our prior work leveraged LiDAR intensity metrics to quantify and reduce incorrect feature extraction risk between pre-defined landmarks equipped with strong retro-reflectors and obstacles under a daytime scenario. However, LiDAR intensity is affected by weather conditions, showing correlations to water droplet density and solar radiation. We quantify the weather-affected LiDAR feature extraction risk using experimental data. Our results indicate that there is no significant increase in incorrect extraction risk under adverse weather conditions when the system incorporates landmarks with strong retro-reflectors that enhance the signal intensity returned to the LiDAR.

## I. INTRODUCTION

We have examined fault-free integrity navigation subject to proposed driverless vehicle requirements. Our investigation showed that alternative position reference updates are required in urban environments where global navigation satellite system (GNSS) signals are frequently obstructed, even if the vehicle is equipped with high-quality inertial and odometry sensors and vehicle kinematic constraints are exploited (Nagai et al., 2022).

To regain some control over navigation performance in challenging environments, we consider augmentation by local ranging using light detection and ranging (LiDAR). LiDAR sensors detect objects in the surrounding space and measure the ranges and angles of those within their field of view. Then, the detected data points are associated with pre-defined landmarks, the locations of which are stored in a database accessible to the vehicle (Levinson et al., 2007). The mapped landmark locations and LiDAR measurements enable the vehicle to estimate its position.

Although all objects in urban environments are candidates for external ranging sources for LiDAR, we specifically focus on extracting pole-like landmarks (e.g., street lamps) because of their location flexibility, relative ubiquity, and defined shapes, as demonstrated in Sefati et al. (2017) and Teo and Chiu (2015). In addition, the laser-based navigation system can achieve centimeter-level accuracy under nominal conditions (Levinson et al., 2007; Wan et al., 2018).

Unfortunately, LiDAR navigation systems may not always operate nominally, and undetected faults in landmark identification can threaten localization safety. LiDAR-based navigation requires two intermediary procedures for positioning from a raw LiDAR scan: feature extraction and data association (see Fig. 1). Faults can occur during both procedures (Bar-Shalom and Fortmann, 1988).

The feature extraction process involves identifying registered landmarks from raw data points. Incorrect extraction (IE) faults occur when the system wrongly identifies irrelevant ‘obstacles’ as landmarks. Then, even if the extraction is correct, uncertainty regarding the source of each measurement can lead to an incorrect association (IA), resulting in a mismatch between the measurement observations and their corresponding locations in the database.

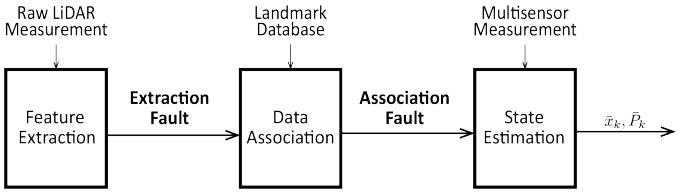


**Figure 1:** The estimation process for a LiDAR-based navigation system. Faults can occur during the feature extraction or data association processes, threatening state estimation integrity.

The method detailed in Joerger et al. (2016) establishes the upper limits for the risk of incorrect associations (IA), and this risk diminishes as the distance between landmarks increases. However, this condition holds only when the system correctly extracts features. Therefore, in (Nagai et al., 2023) we developed a method to quantify feature extraction risk that used retro-reflectors on desired landmarks to enhance the intensity of returned signals. These high-intensity signals can be differentiated from surrounding obstacles that return low-intensity signals. Our experiments demonstrated that the probability of IE is exceedingly low under clear weather daytime conditions.

Performance degradation of LiDAR in adverse weather is well-documented, as noted in studies by Levinson et al. (2007); Filgueira et al. (2017); Heinzler et al. (2019). Wet surfaces reflect less laser light than dry surfaces because of laser beam attenuation and scattering. These studies have discussed sensor performance deterioration but have not evaluated the resulting impacts on navigation safety. The extent to which reduced reflectivity affects safety remains unknown, and this research aims to quantify safety by evaluating the risk in different weather scenarios.

Following this introduction, Section II defines the faults and formulates the integrity risk equation. Section III examines the risk of feature extraction, supported by LiDAR intensity measurements. Section IV addresses the experimental setup, results, and analysis. Finally, Section V is our conclusion.

## II. INTEGRITY RISK OF LIDAR POSITIONING ESTIMATION

### 1. Fault Definitions

We employ successive hypothesis analysis to determine if the system based on LiDAR positioning is operating correctly. The binary hypothesis problem for feature extraction is

$$\begin{cases} H_0 : \text{correct extraction, } P(CE) \\ H_1 : \text{incorrect extraction, } P(IE) \end{cases} \tag{1}$$

where $P(CE)$ defines the probability of the extracted feature *having* a corresponding landmark in the database, and $P(IE)$ defines the probability of the extracted feature *not having* a corresponding landmark in the database.

Since the data association follows the feature extraction, the hypotheses of the association process involve conditional probabilities. We refer to these as successive binary hypotheses. The binary hypothesis problem for data association given correct extraction is

$$\begin{cases} H_0 : \text{correct association given CE, } P(CA|CE) \\ H_1 : \text{incorrect association given CE, } P(IA|CE) \end{cases} \tag{2}$$

where $P(CA|CE)$ denotes the probability that the correctly extracted feature is associated with the *correct* landmark position, and $P(IA|CE)$ indicates the probability that the correctly extracted feature is associated with the *incorrect* landmark position.

Given an incorrect extraction, we have

$$\begin{cases} H_0 : \text{correct association given } IE, P(CA|IE) \\ H_1 : \text{incorrect association given } IE, P(IA|IE) \end{cases} \tag{3}$$

where $P(CA|IE)$ denotes the probability that the incorrectly extracted feature is associated with the *correct* landmark position. $P(IA|IE)$ represents the probability that an incorrectly extracted feature is associated with the *incorrect* landmark position. In our analysis, $P(CA|IE)$ is set to zero because an incorrectly extracted feature can never be associated correctly. The overview of the fault definitions is in Table 1.

**Table 1:** Fault Definitions of LiDAR Positioning System

| Feature Extraction | Data Association |
|---|---|
| $P(H_0) = P(CE)$ | $P(H_0) = P(CA\|CE)$ |
| | $P(H_1) = P(IA\|CE)$ |
| $P(H_1) = P(IE)$ | $P(H_0) = P(CA\|IE) = 0$ |
| | $P(H_1) = P(IA\|IE) \stackrel{\text{def}}{=} 1$ |

We quantify the safety of the navigation system and derive the integrity risk equation represented by the probability of hazardously misleading information $P(HMI)$. From the law of total probability, the integrity risk is

$$P(HMI) = P(HMI|H_0)P(H_0) + P(HMI|H_1)P(H_1) \tag{4}$$

where $P(H_0)$ and $P(H_1)$ are the prior probability of each of the two mutually exclusive hypotheses. $P(HMI|H_0)$ and $P(HMI|H_1)$ are the corresponding risks of hazardously misleading information (i.e., excessive position estimate error). Considering the feature extraction procedure defined in (1), (4) can be replaced by the following:

$$P(HMI) = P(HMI|CE)P(CE) + P(HMI|IE)P(IE). \tag{5}$$

Considering the data association process given $CE$ in (2), $P(HMI|CE)$ becomes

$$P(HMI|CE) = P(HMI|CA, CE)P(CA|CE) + P(HMI|IA, CE)P(IA|CE). \tag{6}$$

Since the position error resulting from an $IE$ and $IA$ is unknown, we upper bound the conditional probabilities of $HMI$ in these cases as 1:

$$P(HMI|IE) \stackrel{\text{def}}{=} 1 \tag{7}$$

$$P(HMI|IA, CE) \stackrel{\text{def}}{=} 1 \tag{8}$$

Due to the mutually exclusive conditions presented in (1) and (2), we can express $P(IE)$ and $P(IA|CE)$ using the following equations.

$$P(IE) = 1 - P(CE) \tag{9}$$

$$P(IA|CE) = 1 - P(CA|CE) \tag{10}$$

Combining (5)-(10), the integrity risk upper bound is

$$P(HMI) \leq 1 - [1 - P(HMI|CA, CE)]P(CA|CE)P(CE). \tag{11}$$

Equation (11) does not take the concept of time into account. Considering the integrity risk at time index $n$, we rewrite (11) as:

$$P(HMI_n) \leq 1 - [1 - P(HMI_n|CA_N, CE_N)]P(CA_N|CE_N)P(CE_N) \tag{12}$$

where $N$ denotes a range of time indices $N = \{1, 2, ...n\}$. To simplify upcoming calculations, the equation conservatively (but not unrealistically) assumes that past incorrect extraction or association events result in current $HMI$.

The probabilities of correct association and extraction for all times are (Joerger et al., 2016):

$$P(CA_N|CE_N) \stackrel{\text{def}}{=} \prod_{j=1}^{n} P(CA_j|CE_J, CA_{J-1}) \tag{13}$$

$$P(CE_N) \stackrel{\text{def}}{=} \prod_{j=1}^{n} P(CE_j|CE_{J-1}) \tag{14}$$

where $J$ denotes a range of time indices $J = \{1, 2, ...j\}$. Equations (13) and (14) define the probabilities of all past extraction and association events being correct.

We aim to reduce the integrity risk defined in (12), which comprises position error, association, and extraction faults, to meet the driverless vehicle integrity requirements for urban environments specified in Table 2.

**Table 2:** The integrity required for driverless vehicles in urban environments

| | **upper** (EUSPA, 2021) | **lower** (Reid et al., 2019) |
|---|---|---|
| availability | $> 99.9\%$ | $(> 99.9\%)$ |
| protection level | $(< 10^{-7}$ per moment) | $< 10^{-8}$ per moment |
| alert limit ($l$) | $(< 0.5$ m) | $< 0.3$ m |
| max. allowable position std. dev. ($1\sigma$) | $< 0.1$ m | $< 0.05$ m |

( ) represents a value used in our analysis but not specified in the cited paper.

### 2. Integrity Risk Due to Position Estimate Error

The probability of a fault-free position error, denoted by $P(HMI_n|CA_N, CE_N)$ in (12), can be calculated using the variance of the position state:

$$P(HMI_n|CA_N, CE_N) = 2\Phi[-l/\sigma_n]. \tag{15}$$

where $\Phi[\cdot]$ is the standard normal cumulative distribution function (CDF), $l$ is the alert limit, and $\sigma_n$ is the standard deviation of the position error in the direction of interest at time epoch $n$. Given the integrity requirements in Table 2, the maximum allowable position error standard deviation (i.e., maximum $\sigma_n$) is 0.05 m at the lower limit and 0.1 m at the upper limit.

Our simulation results presented in Nagai et al. (2022) demonstrated that a navigation system integrating four GNSS constellations, a high-quality INS, wheel speed sensors, and vehicle kinematic constraints was insufficient to meet the integrity requirements in Table 2 in a representative urban environment: downtown Chicago. However, when the system was augmented with LiDAR positioning with landmark intervals at approximately 14 meters or less, even the lower limit integrity requirements were achievable.

### 3. Integrity Risk Due to Incorrect Feature Association

GNSS utilizes pseudo-random noise (PRN) coding to associate observation data with navigation data; conversely, LiDAR measurements do not have a tagging system that connects a pair of LiDAR measurements with the corresponding landmark location in the database. The nearest neighbor algorithm has been employed (Bar-Shalom and Fortmann, 1988), which selects the optimal pair based on the smallest Mahalanobis distance, to address this association issue. However, this approach can result in incorrect associations $P(IA|CE)$ in (2) due to measurement noise and a-priori state estimate errors when landmarks are close to each other.

Joerger et al. (2016) and Hassani and Joerger (2023) derived a lower bound on $P(CA_j|CE_J, CA_{J-1})$ for the nearest neighbor algorithm. Using this result, we showed in Nagai et al. (2023), for the same downtown Chicago case study in Nagai et al. (2022), that when both ranging and bearing LiDAR measurements are used for feature association, a minimum landmark spacing of approximately two meters was sufficient to ensure that $P(IA_j|CE_J, CA_{J-1}) = 1 - P(CA_j|CE_J, CA_{J-1})$ is negligibly small.

## III. FEATURE EXTRACTION RISK

### 1. Methodology

Extracting landmarks from a large amount of LiDAR data points while minimizing extraction faults is challenging. The coarse-to-fine approach, which involves initially identifying landmarks from larger segments and subsequently focusing on smaller point scales, has been studied to address this issue (Teo and Chiu, 2015; Golovinskiy et al., 2009). Although height, position, and shape information have been suggested to filter points belonging to poles, here we focus on intensity filtering. We treat the decision-making process regarding whether points belong to a landmark as binary hypothesis problem, in this case guided by the likelihood of observing the LiDAR measurements $z$ under each hypothesis. This hypothesis test is conducted using the Neyman-Pearson lemma.

Given that there are typically more obstacles than landmarks in an environment, we define the two hypotheses as follows:

$$\begin{cases} H_0 : \text{obstacle (non-reflective object)} \\ H_1 : \text{landmark (reflective object).} \end{cases} \tag{16}$$

The likelihood function are probability density of the normal distribution is expressed as

$$\begin{cases} p(z|H_0) = \frac{1}{\sqrt{2\pi\sigma_0^2}}\exp(-\frac{1}{2\sigma_0^2}(z-\mu_0)^2) \\ p(z|H_1) = \frac{1}{\sqrt{2\pi\sigma_1^2}}\exp(-\frac{1}{2\sigma_1^2}(z-\mu_1)^2) \end{cases} \tag{17}$$

where $\sigma$ is the intensity standard deviation, and $\mu$ is the mean. The likelihood ratio test is

$$\Lambda(z) = \frac{p(z|H_1)}{p(z|H_0)} \underset{H_0}{\overset{H_1}{\gtrless}} \gamma \tag{18}$$

where $\gamma$ is a constant threshold whose possible values will be discussed later. We define $IE$ from the four possible decisions:

1. pick $H_0$ given $H_0 \rightarrow$ correct = no integrity threat
2. pick $H_0$ given $H_1 \rightarrow$ no-extraction ($NE$) = no integrity threat
3. pick $H_1$ given $H_1 \rightarrow$ correct = no integrity threat
4. pick $H_1$ given $H_0 \rightarrow$ incorrect extraction ($IE$) = integrity threat.

Using the Neyman-Pearson Lemma, the $IE$ risk per epoch can be calculated as follows

$$P(IE_j|CE_{J-1}) = \int_{\{z:\wedge(z)>\gamma\}} p\left(z|\mathcal{H}_0\right) dx. \tag{19}$$

We define the mutually exclusive hypothesis in (1), and the probability of correct extraction becomes

$$P(CE_j|CE_{J-1}) = 1 - \int_{\{z:\wedge(z)>\gamma\}} p\left(z|\mathcal{H}_0\right) dx. \tag{20}$$

The NE event per epoch can be calculated as follows

$$P(NE_j|CE_{J-1}) = \int_{\{z:\wedge(z)<\gamma\}} p\left(z|\mathcal{H}_1\right) dx. \tag{21}$$

The values from $\mu$ and $\sigma$ in (17) can be obtained from experimental data, which may be subject to the influence of weather conditions.

### 2. Urban Environment Control

Based on our prior findings, urban environments designed to minimize integrity risk must meet three criteria. Firstly, to decrease the fault-free position error, the landmarks should not be spaced too far apart (e.g., in our downtown Chicago case study, no more than 14 meters). Secondly, to lower the association risk, landmarks should be not be spaced too closely (at least 2 meters apart in the Chicago case study). Lastly, landmarks should exhibit unique likelihood functions, distinct from generic obstacles, to make extraction decisions correctly.

A LiDAR sensor captures intensity information by measuring the number of reflected photons returned from features. The properties of the feature surface determine the numbers, which can be used to classify features based on their unique intensity distributions (Kashani et al., 2015). In our work, we wrap reflective tape around landmarks to amplify the intensity of their laser returns. We employ the number of returned photons as the intensity metric for landmark decisions. The intensity distributions will be derived from experimental results discussed in the following section.

## IV. EXPERIMENT EXAMINING THE IMPACT OF WEATHER ON LIDAR INTENSITY

### 1. Experimental Setup

An experiment was conducted to collect data in March and April 2023 at Argonne National Laboratory in Lemont, Illinois. The setup was comprised of a Vaisala Forward Scatter Sensor FD70 for measuring precipitation intensity and a high-fidelity Ouster OS2 LiDAR with 128-channel resolution. Each LiDAR return 'point' has position and intensity information, the latter quantified

by the number of returned photons. The LiDAR sensor observed a reflective object (i.e., a stop sign) and a non-reflective object (i.e., a steel object) from a distance. Figure 2 shows the visual image and point clouds of the extracted features. Additionally, solar radiation data for the area was obtained from the World Meteorological Organization (World Meteorological Organization, nd). This information was used to analyze the impact of weather on the LiDAR intensity measurements.


**Figure 2:** (a) Image of the reflective and non-reflective objects. (b) The corresponding LiDAR point cloud generated from the objects.

## 2. Experimental Results - Weather Effects on LiDAR Signal Intensity

We investigate the relationship between weather conditions—quantified by the amount of precipitation and solar radiation—and LiDAR signal intensity. Figure 3 presents a dual-axis time series analysis spanning 24 hours (local time on the x-axis) on March 23, 2023. LiDAR scans were conducted at 5-minute intervals to capture a frame that contains the surrounding scene as a point cloud. The top figure illustrates precipitation in inches per hour, represented by blue bars, and solar radiation in watts per square meter, depicted with yellow bars. The bottom figure displays the maximum and minimum intensity values over the frame for both reflective and non-reflective objects.

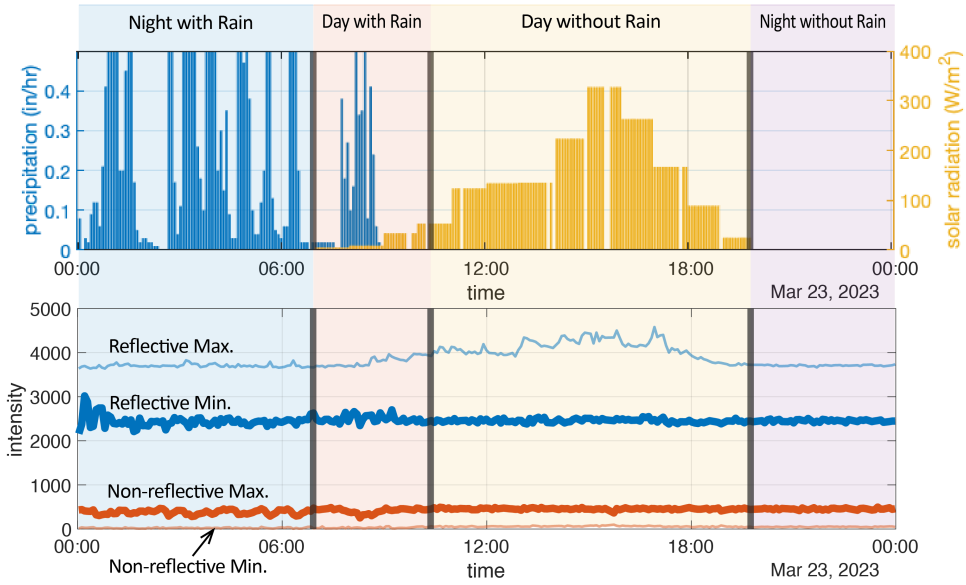


**Figure 3:** (Top) Precipitation in blue and solar radiation in yellow bars over 24 hours. (Bottom) Maximum and minimum LiDAR intensity over the frame.

As many studies have noted, weather conditions can influence the intensity of LiDAR returns. Figure 3 shows spikes in the precipitation bars during the morning, indicative of intermittent rainfall, and these spikes make the LiDAR intensity fluctuate. Additionally, increases in the height of the yellow bars, representing more intense solar radiation, correspond to the maximum intensity value of the reflective object. While weather conditions do affect LiDAR intensity values, the factor affecting extraction decisions is the intensity difference between the minimum values of reflective objects and the maximum values of non-reflective objects. This difference, as exhibited in Figure 3, is sufficient to prevent incorrect extractions; the probabilistic analysis leading to this assertion is described in the following section.

## 3. Experimental Results - Feature Extraction Risk

We have classified weather conditions into four scenarios: night with rain, day with rain, night without rain, and day without rain. Figure 4 illustrates the intensity histograms for each scenario, considering both reflective and non-reflective objects.

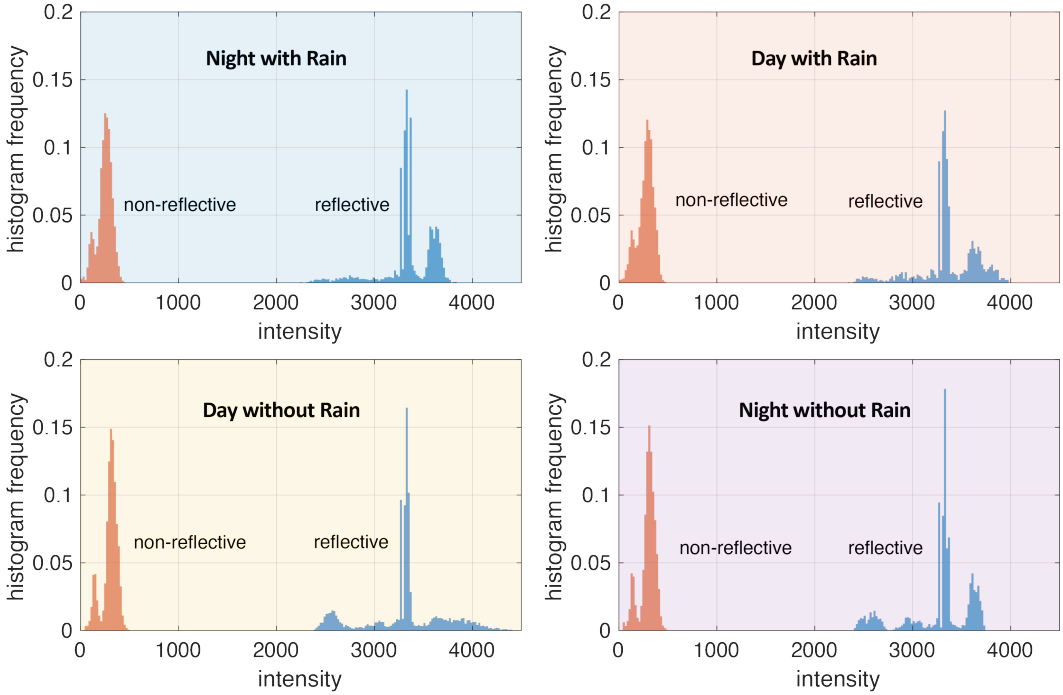


**Figure 4:** Four histogram plots showing LiDAR intensity measurements for reflective and non-reflective objects under different weather conditions.

We employ Gaussian distributions to overbound the empirical CDFs (DeCleene, 2000; Rife et al., 2006) and compute integrity risks at probabilities lower than retrievable from the empirical CDFs directly. Figure 5 shows an example of these overbounds. Table 3 details the mean ($\mu$) and standard deviation ($\sigma$) values of the bounding Gaussian distributions.

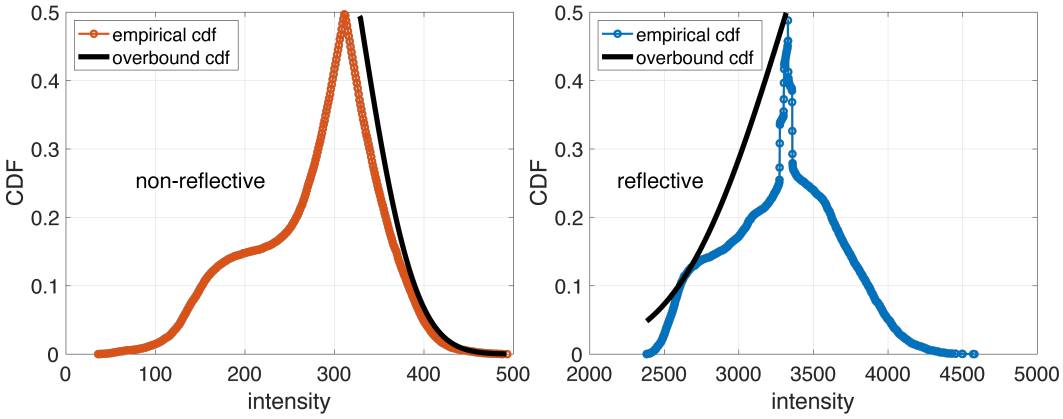


**Figure 5:** Gaussian overbounds: Gaussian distributions that upper bound integrity risk of the empirical distributions.

We evaluate landmark incorrect extraction ($IE$) risk using the overbounding Gaussian distributions; the results are shown in Figure 6. The x-axis shows possible rejection thresholds and the y-axis the corresponding risk level. The four curves represent the different weather scenarios. The results suggest that setting a rejection threshold on intensity of 800 would lead to $IE$ risk lower than $10^{-14}$.

Figure 7 shows no-extraction ($NE$) risk. These events occur when the system erroneously rejects a landmark, mistaking it for

**Table 3:** The mean ($\mu$) and standard deviation ($\sigma$) values of the signal intensity photons for bounded Gaussian distributions.

| material | condition | $\mu$ | $\sigma$ |
|---|---|---|---|
| reflective | night with rain | 3362 | 408 |
| | day with rain | 3393 | 404 |
| | day without rain | 3318 | 563 |
| | night without rain | 3271 | 505 |
| non-reflective | night with rain | 283 | 51 |
| | day with rain | 306 | 53 |
| | day without rain | 328 | 48 |
| | night without rain | 326 | 48 |

an obstacle. If the rejection threshold is below 1000, the probability of a no-extraction event is below $10^{-5}$ in the worst-case weather scenario.

From the results, when the threshold is between 800 and 1000, the system sets sufficient separation to mitigate $IE$ risk and simultaneously limit the no-extraction events. This finding suggests that weather conditions become less relevant when the LiDAR navigation system relies on intensity measurements for feature detection.

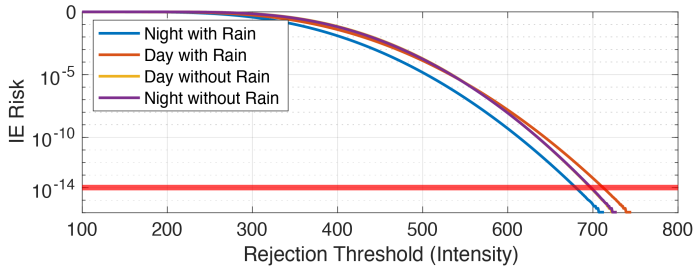


**Figure 6:** The plot demonstrates the relationship between the rejection threshold and incorrect extraction risk under various environmental conditions. The risk falls below $10^{-14}$ when the rejection threshold exceeds 800.

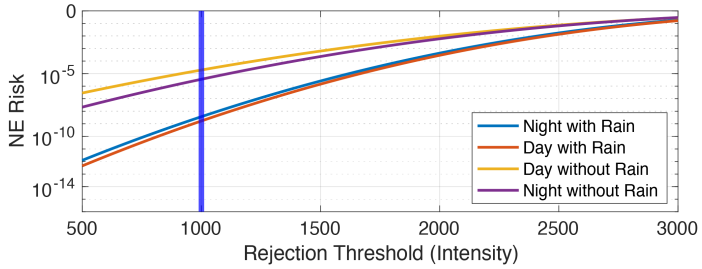


**Figure 7:** The plot illustrates the relationship between the rejection threshold and no-extraction event. In the worst-case scenario, this risk falls below $10^{-5}$ when the rejection threshold is set below 1000.

Future studies should further investigate no-extraction events. While they do not pose integrity threats, they do result in an sparseness in effective landmark density, which may require a decrease in landmark spacing to maintain navigation availability.

## V. CONCLUSION

This study examines the integrity risk in LiDAR-based navigation for driverless vehicles as determined by positioning accuracy, landmark incorrect association ($IA$), and incorrect extraction ($IE$) risks. It specifically explores how adverse weather impacts $IE$ risk by analyzing the differing intensity responses of reflective and non-reflective objects. Heavy rain and solar radiation influence the reflectivity, but these weather impacts on intensity metrics for feature extraction are limited. The results show that

reflective and non-reflective objects are still easily distinguishable with low $IE$ risk. Future studies should explore no-extraction ($NE$) events, where the system mistakenly rejects landmarks as obstacles, leading to reduced landmark density and potential degradation of LiDAR navigation availability.

## ACKNOWLEDGEMENTS

This article is based on work supported by the Center for Assured and Resilient Navigation in Advanced TransportatION Systems (CARNATIONS) under the US Department of Transportation (USDOT)'s University Transportation Center (UTC) program (Grant No. 69A3552348324). Any opinions, findings, and conclusions or recommendations expressed in this paper are those of the authors and do not necessarily reflect the views of the sponsors.

## REFERENCES

Bar-Shalom, Y. and Fortmann, T. (1988). *Tracking and Data Association*. Mathematics in Science and Engineering. Academic Press.

DeCleene, B. (2000). Defining pseudorange integrity-overbounding. In *Proceedings of the 13th International Technical Meeting of the Satellite Division of The Institute of Navigation (ION GPS 2000)*, pages 1916–1924.

EUSPA (2021). Report on road user needs and requirements. https://www.gsc-europa.eu.

Filgueira, A., González-Jorge, H., Lagüela, S., Díaz-Vilariño, L., and Arias, P. (2017). Quantifying the influence of rain in LiDAR performance. *Measurement*, 95:143–148. https://doi.org/10.1016/j.measurement.2016.10.009.

Golovinskiy, A., Kim, V. G., and Funkhouser, T. (2009). Shape-based recognition of 3D point clouds in urban environments. In *2009 IEEE 12th International Conference on Computer Vision*, pages 2154–2161. IEEE. https://doi.org/10.1109/ICCV.2009.5459471.

Hassani, A. and Joerger, M. (2023). Analytical and empirical navigation safety evaluation of a tightly integrated LiDAR/IMU using return-light intensity. *Navigation: Journal of the Institute of Navigation*, 70(4). https://navi.ion.org/content/70/4/navi.623.

Heinzler, R., Schindler, P., Seekircher, J., Ritter, W., and Stork, W. (2019). Weather influence and classification with automotive lidar sensors. In *2019 IEEE Intelligent Vehicles Symposium (IV)*, pages 1527–1534. IEEE. https://doi.org/10.1109/IVS.2019.8814205.

Joerger, M., Jamoom, M., Spenko, M., and Pervan, B. (2016). Integrity of laser-based feature extraction and data association. In *2016 IEEE/ION Position, Location and Navigation Symposium (PLANS)*, pages 557–571. IEEE. https://doi.org/10.1109/PLANS.2016.7479746.

Kashani, A. G., Olsen, M. J., Parrish, C. E., and Wilson, N. (2015). A review of LiDAR radiometric processing: From ad hoc intensity correction to rigorous radiometric calibration. *Sensors*, 15(11):28099–28128. https://doi.org/10.3390/s151128099.

Levinson, J., Montemerlo, M., and Thrun, S. (2007). Map-based precision vehicle localization in urban environments. In *Robotics: Science and Systems*, volume 4, page 1. Atlanta, GA, USA. https://doi.org/10.15607/RSS.2007.III.016.

Nagai, K., Chen, Y., Spenko, M., Henderson, R., and Pervan, B. (2023). Integrity with extraction faults in LiDAR-based urban navigation for driverless vehicles. In *2023 IEEE/ION Position, Location and Navigation Symposium (PLANS)*, pages 1099–1106. IEEE. https://doi.org/10.1109/PLANS53410.2023.10140132.

Nagai, K., Spenko, M., Henderson, R., and Pervan, B. (2022). Fault-free integrity and continuity for driverless urban vehicle navigation with multi-sensor integration: A case study in downtown Chicago. In *Proceedings of the 35th International Technical Meeting of the Satellite Division of The Institute of Navigation (ION GNSS+ 2022)*, pages 1350–1365. https://doi.org/10.33012/2022.18319.

Reid, T. G., Houts, S. E., Cammarata, R., Mills, G., Agarwal, S., Vora, A., and Pandey, G. (2019). Localization requirements for autonomous vehicles. *SAE International Journal of Connected and Automated Vehicles*, 2(3):1–16. https://doi.org/10.4271/12-02-03-0012.

Rife, J., Pullen, S., Enge, P., and Pervan, B. (2006). Paired overbounding for nonideal laas and waas error distributions. *IEEE Transactions on Aerospace and Electronic Systems*, 42(4):1386–1395.

Sefati, M., Daum, M., Sondermann, B., Kreisköther, K. D., and Kampker, A. (2017). Improving vehicle localization using semantic and pole-like landmarks. In *2017 IEEE Intelligent Vehicles Symposium (IV)*, pages 13–19. IEEE. https://doi.org/10.1109/IVS.2017.7995692.

Teo, T.-A. and Chiu, C.-M. (2015). Pole-like road object detection from mobile lidar system using a coarse-to-fine approach. *IEEE Journal of Selected Topics in Applied Earth Observations and Remote Sensing*, 8(10):4805–4818. https://doi.org/10.1109/JSTARS.2015.2467160.

Wan, G., Yang, X., Cai, R., Li, H., Zhou, Y., Wang, H., and Song, S. (2018). Robust and precise vehicle localization based on multi-sensor fusion in diverse city scenes. In *2018 IEEE International Conference on Robotics and Automation (ICRA)*, pages 4670–4677. IEEE. https://doi.org/10.1109/ICRA.2018.8461224.

World Meteorological Organization (n.d.). https://wmo.int/.